A climatological assessment of intense extratropical cyclones from the potential vorticity perspective

Christian Seiler

2019

Original citation:

Seiler, C. (2019). A climatological assessment of intense extratropical cyclones from the potential vorticity perspective. *Journal of Climate*, *32*(8), 2369–2380. https://doi.org/10.1175/JCLI-D-18-0461.1

A Climatological Assessment of Intense Extratropical Cyclones from the Potential Vorticity Perspective

CHRISTIAN SEILER[a]

Pacific Climate Impacts Consortium, University of Victoria, and Climate Processes Section, Science and Technology Branch, Environment and Climate Change Canada, Victoria, British Columbia, Canada

(Manuscript received 20 July 2018, in final form 8 February 2019)

Extratropical cyclones (ETCs) are known to intensify due to three vertically interacting positive potential vorticity perturbations that are associated with potential temperature anomalies close to the surface (θ_B), condensational heating in the lower-level atmosphere (q_{sat}), and stratospheric intrusion in the upper-level atmosphere (q_{tr}). This study presents the first climatological assessment of how much each of these three mechanisms contributes to the intensity of extreme ETCs. Using relative vorticity at 850 hPa as a measure of ETC intensity, results show that in about half of all cases the largest contributions during maximum ETC intensity are associated with q_{sat} (53% of all ETCs), followed by q_{tr} (36%) and θ_B (11%). The relative frequency of storms that are dominated by q_{sat} is higher 1) during warmer months (61% of all ETCs during warmer months) compared to colder months (50%) and 2) in the Pacific (56% of all ETCs in the Pacific) compared to the Atlantic (46%). The relative frequency of ETCs that are dominated by θ_B is larger 1) during colder months (13%) compared to warmer months (3%), 2) in the Atlantic (15%) compared to the Pacific (8%), and 3) in western (11%–20%) compared to eastern ocean basins (4%–9%). These findings are based on piecewise potential vorticity inversion conducted for intense ETCs that occurred from 1980 to 2016 in the Northern Hemisphere (3273 events; top 7%). The results may serve as a baseline for evaluating ETC biases and uncertainties in global climate models.

1. Introduction

Extratropical cyclones (ETCs) play an important role in Earth's climate system as they exchange heat, moisture, and momentum between the tropics and the higher latitudes. They also generate extreme surface wind speeds and heavy precipitation events with frequent devastating impacts on human activities and infrastructure (Fink et al. 2009). Understanding the dynamics of these events under current and future climate conditions is, therefore, of great scientific and public interest (Ulbrich et al. 2009). The dynamics of ETCs can be assessed from the potential vorticity (q) perspective, which is outlined next.

Cyclogenesis is driven by the interaction of an upper-level disturbance, surface baroclinicity, and diabatic heating in the middle atmosphere (Davis and Emanuel 1991). An upper-level positive potential vorticity anomaly (q') can form during a tropopause fold that causes intrusion of stratospheric air (Whitaker et al. 1988). The cyclonic circulation associated with the upper-level positive q' penetrates down the troposphere and induces a weak cyclonic circulation close to the surface (Hoskins et al. 1985). This deforms the low-level isotherms through horizontal temperature advection, with warm air advecting to the north and east and cold air advecting to the south and west in the Northern Hemisphere (NH), leading to a warm surface potential temperature anomaly (θ') located to the east of the upper-level positive q' (Martin 2013). This warm surface θ' acts as a surrogate positive q' and creates its own cyclonic circulation that penetrates upward and intensifies the upper-level positive q'. When the vertical axis between both anomalies is tilted westward with height, the positive upper-level q' and positive surface q' become phase locked, allowing for mutual amplification and cyclogenesis (Gray and Dacre 2006). Diabatic heating in the midtroposphere enhances this mutual amplification

---

Denotes content that is immediately available upon publication as open access.

---

[a] Current affiliation: Climate Processes Section, Science and Technology Branch, Environment and Climate Change Canada, Victoria BC, Canada.

Corresponding author: Christian Seiler, christian.seiler@canada.ca

DOI: 10.1175/JCLI-D-18-0461.1

by increasing the penetration depth through a reduction of static stability, and by q production in the lower-level atmosphere and q destruction in the upper-level atmosphere (Stoelinga 1996). The latter process intensifies the upper-level positive q' since this anomaly is located west of the lower-level positive q', while the region of q destruction is located directly above the lower-level positive q'. Once the ETC reaches its maximum intensity, all three positive q anomalies become vertically aligned. The role of upper-level disturbance, surface baroclinicity, and diabatic heating vary among ETCs, which lead to the distinction of three ETC types (Petterssen and Smebye 1971; Deveson et al. 2002; Dacre and Gray 2009). More recent work by Graf et al. (2017) finds that cyclogenesis events form a continuum rather than a set of distinct types.

A climatological assessment by Čampa and Wernli (2012) shows that 1) stronger ETCs have larger values of surface θ' and q' than weaker ETCs, 2) surface θ' and lower-level q' are greater in western than in eastern parts of the North Pacific and Atlantic, and 3) surface θ' is larger during NH winter compared to NH summer. The contributions of θ' and q' to ETC intensification can be assessed through piecewise potential vorticity inversion (PPVI) (Davis and Emanuel 1991). The technique is based on the invertibility of q, which makes it possible to derive wind and geopotential height fields for an appropriate set of balance and boundary conditions (Hoskins et al. 1985). PPVI partitions q' into distinct layers, such as a surface layer, a lower atmospheric layer, and an upper atmospheric layer (Davis and Emanuel 1991). Using relative humidity as an additional criterion next to pressure to partition q' makes it possible to associate contributions with boundary θ' close to the surface (θ_B), condensational heating in the lower-level atmosphere (q_{sat}), and stratospheric intrusion in the upper-level atmosphere (q_{tr}) (Davis 1992).

Previously published case studies suggest that the relative importance of these mechanisms strongly varies among ETCs, where ETC intensification can be dominated by θ_B (50%) (Davis 1992), q_{sat} (70%) (Stoelinga 1996), and q_{tr} (53%) (Huo et al. 1999), or where all mechanisms contribute equally to ETC intensity (Martin and Otkin 2004). It remains unclear how frequently ETCs are dominated by θ_B, q_{sat}, and q_{tr} and how such frequencies vary among seasons and regions. Filling this gap could help to identify the underlying causes of ETC biases and uncertainties in global climate models (GCMs).

GCMs tend to underestimate ETC intensity and show substantial uncertainties concerning the future response of the North Atlantic storm track to increased greenhouse gas (GHG) concentrations (Zappa et al. 2013a; Collins et al. 2013; Seiler and Zwiers 2016a,b). Previous attempts to identify the sources of ETC biases and uncertainties include mainly idealized model experiments and statistical approaches (Lunkeit et al. 1998; Butler et al. 2010; Woollings et al. 2012; Zappa et al. 2013a,b; Seiler and Zwiers 2016a,b). The first method, however, cannot easily be implemented for a multi-GCM ensemble and the second approach cannot fully prove causality or disentangle dynamically interacting mechanisms. PPVI overcomes these limitations and may, therefore, provide new ways to explore ETC bias and uncertainties in GCMs. This study presents the first PPVI-based climatology for intense ETCs in the Northern Hemisphere. The results may serve as a baseline for evaluating ETC biases and uncertainties in GCMs.

The following section presents the data and approach used for ETC tracking and PPVI. Section 3 shows 1) the selection of intense ETCs considered in this study, 2) the potential vorticity structure of these storms, 3) the contributions to ETC intensity from different pressure levels, 4) the sensitivity of these contributions to different methodological settings, and 5) contributions associated with θ_B, q_{sat}, and q_{tr}. Section 4 elaborates on the principal findings and discusses how PPVI can be used for assessing ETC biases and uncertainties in GCMs.

2. Methods

a. Data

This analysis uses the ERA-Interim (Dee et al. 2011), which is based on a spectral model with T255 truncation and 60 vertical levels. The data are converted to a 480 × 240 (0.75°; 83 km) horizontal linear grid for the ETC tracking and to a 144 × 72 (2.5°; 278 km) horizontal linear grid for PPVI. The input data for ETC tracking consist of global 6-hourly horizontal wind speeds at 850 hPa. The data used for PPVI include 12-hourly values of geopotential height, air temperature, and zonal and meridional wind speed at 1000, 850, 700, 500, 400, 300, 250, 200, 150, and 100 hPa. All data cover the period 1980 to 2016.

b. Cyclone tracking

ETCs are identified using the objective feature tracking algorithm TRACK (Hodges 1994; Hodges et al. 1995; Hodges 1999). The algorithm computes the vertical component of relative vorticity from the horizontal wind velocity at 850 hPa (ζ_{850}) at the resolution of the input data. I then spatially filter ζ_{850} to T42 resolution (T42ζ_{850}) prior to tracking through spherical harmonic decomposition (Anderson et al. 2003). Feature points are detected based on local extreme values. The algorithm computes ETC tracks by determining the correspondence between feature points for adjacent time steps. Post-tracking filters are applied to retain only storms that have a T42ζ_{850} greater than $10^{-5}\,\mathrm{s}^{-1}$, that last longer than two days, and that travel farther than 1000 km, which leads to 49 165 ETCs that occurred from 1980 to 2016. Intense ETCs are here defined as storms that have at least one ETC center with T42$\zeta_{850} \geq 10 \times 10^{-5}\mathrm{s}^{-1}$, which applies to 3431 events, or 7% of all ETCs. ETC centers that are south of 30° latitude or north of 72° latitude are excluded (Fig. 1). While the southern limit avoids tropical systems, the northern limit avoids having the meridional borders of the inversion domain converge close to the pole. The latter occurs because the inversion domain consists of a rectangle that extends 15° latitude north and south, and 20° longitude east and west of the ETC center of interest. If the ETC is north of 72°N then the upper limit of the inversion domain reaches the North Pole, and a rectangular domain can no longer be formed. Finally, I also excluded ETC centers that occur during the first or last 3 days of a year due to the computation of a 5-day mean that is centered at each of the four time steps of an ETC track considered in this study. This is necessary as ETCs are computed from annual data. These measures reduce the total number of intense ETCs considered in this study to 3273. The majority (78%) of these ETCs occur during the colder part of the year from October to March.

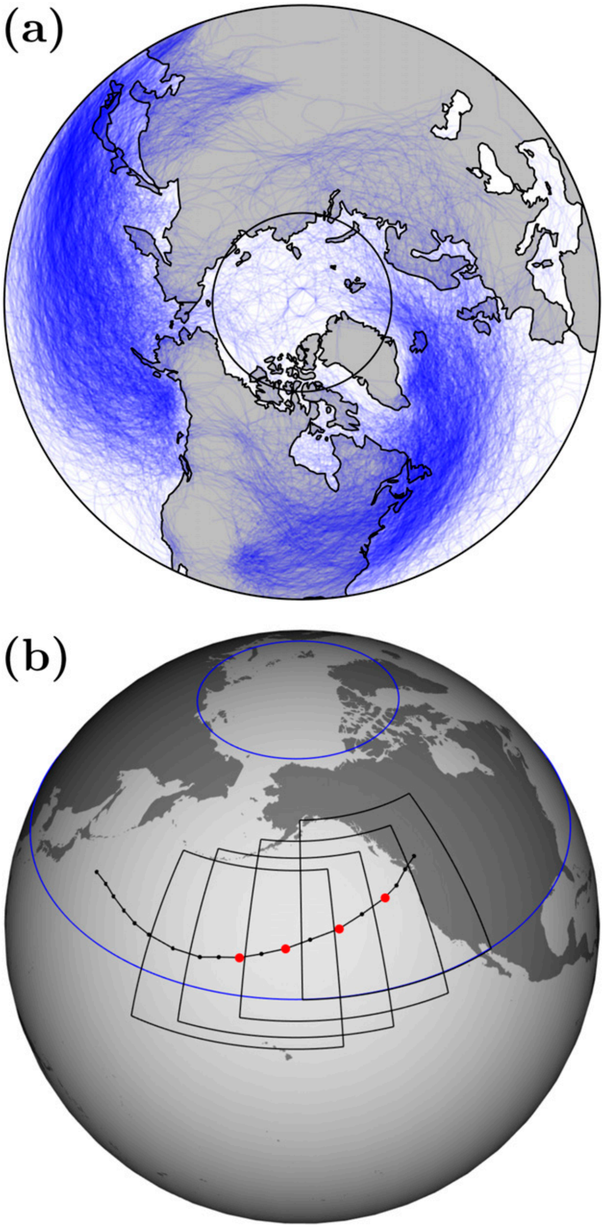

Fig. 1. (a) All ETC tracks from 1980 to 2016 with maximum T42$\zeta_{850} \geq 10 \times 10^{-5}\,\mathrm{s}^{-1}$ (3431 tracks), and (b) spatial domains used for PPVI applied to four ETC centers for an example ETC track (Hanukkah Eve Storm in December 2006; Mass and Dotson 2010). The red dots show the ETC centers of a eastward moving storm 36, 24, 12, and 0 h prior to maximum T42ζ_{850}. The blue lines denote 30° and 72°N.

c. *Piecewise potential vorticity inversion*

Ertel potential vorticity q can be inverted to recover geopotential (Φ) and streamfunction (Ψ). This makes it possible to quantify the perturbations of Φ and Ψ at each atmospheric level that contribute to the total perturbation of q at a particular atmospheric level of interest. Inverting q during ETC intensification can, therefore, be used to assess the roles of different mechanisms that drive ETC intensification. This technique is referred to as PPVI and is documented in detail in Davis and Emanuel (1991) and Davis (1992). This section summarizes the main steps that are required to conduct PPVI for ETCs. In this application, I quantify the contribution of each atmospheric layer to T42ζ_{850}, which is my measure of ETC intensity.

Ertel q is defined as the dot product of absolute vorticity ($\boldsymbol{\eta}$) and the three-dimensional gradient of potential temperature θ:

$$q = \frac{1}{\rho}\boldsymbol{\eta} \cdot \nabla\theta, \qquad (1)$$

where ρ is the density. Neglecting vertical velocity and using the Exner function π rather than pressure as a vertical coordinate, Eq. (1) can be rewritten in spherical coordinates (Davis and Emanuel 1991):

$$q = -\frac{g\kappa\pi}{p}\left(\eta\frac{\partial\theta}{\partial\pi} - \frac{1}{a\cos\phi}\frac{\partial v}{\partial\pi}\frac{\partial\theta}{\partial\lambda} + \frac{1}{a}\frac{\partial u}{\partial\pi}\frac{\partial\theta}{\partial\phi}\right), \qquad (2)$$

where a is Earth's radius, g is the gravitational acceleration, λ is the longitude, ϕ is the latitude, and η is the vertical component of $\boldsymbol{\eta}$ written in spherical coordinates.

As a first step I compute q for the entire domain and Φ and Ψ along the boundaries of the domain as an input for lateral and horizontal boundary conditions used during PPVI (Fig. 2). The variables q, Φ, and Ψ are then decomposed into a 5-day time t mean part and a perturbation part: $q(\lambda, \phi, \pi, t) = \overline{q}(\lambda, \phi, \pi) + q'(\lambda, \phi, \pi, t)$. The 5-day time mean presents the background flow, roughly corresponding to one synoptic-scale wave period (Davis 1992). To invert q it is necessary to specify a balance condition that relates Φ and Ψ. The balance condition assumes that the magnitude of the irrotational component of the wind is much smaller than the magnitude of the nondivergent wind ($|\mathbf{v}_\chi| \ll |\mathbf{v}_\psi|$), so that terms involving $\mathbf{v}_\chi$ can be neglected and $\mathbf{v}_\psi = \mathbf{k} \times \nabla\Psi$. In this way, Φ can be expressed as a function of the nondivergent streamfunction Ψ (Davis 1992):

$$\nabla^2\Phi = \nabla \cdot (f\nabla\Psi) + \frac{2}{a^4\cos^2\phi}\left[\frac{\partial^2\Psi}{\partial\lambda^2}\frac{\partial^2\Psi}{\partial\phi^2} - \left(\frac{\partial^2\Psi}{\partial\lambda\,\partial\phi}\right)^2\right]. \tag{3}$$

Using the hydrostatic approximation ($\partial\Phi/\partial\pi = -\theta$) and replacing the horizontal velocity with the nondivergent wind:

$$\left(u = -\frac{1}{a}\frac{\partial\Psi}{\partial\phi} \quad \text{and} \quad v = \frac{1}{a\cos\phi}\frac{\partial\Psi}{\partial\lambda}\right),.$$

Eq. (2) can be rewritten in terms of Ψ and Φ (Davis and Emanuel 1991):

$$q = \frac{g\kappa\pi}{p}\left[(f + \nabla^2\Psi)\frac{\partial^2\Phi}{\partial\pi^2} - \frac{1}{a^2\cos^2\phi}\frac{\partial^2\Psi}{\partial\lambda\,\partial\pi}\frac{\partial^2\Phi}{\partial\lambda\,\partial\pi} - \frac{1}{a^2}\frac{\partial^2\Psi}{\partial\phi\,\partial\pi}\frac{\partial^2\Phi}{\partial\phi\,\partial\pi}\right]. \tag{4}$$

Full q inversion can now be conducted by solving Eqs. (3) and (4) simultaneously for balanced values of Φ and Ψ for a given q [computed in Eq. (2)]. The required boundary conditions are Φ and Ψ on the lateral boundaries (Dirichlet boundary conditions) and their vertical derivatives on the horizontal boundaries (Neumann boundary conditions). Full q inversion is conducted for instantaneous values (q) and for mean values ($\overline{q}$), leading to instantaneous balanced Φ and Ψ, and mean balanced $\overline{\Phi}$ and $\overline{\Psi}$ (Fig. 2).

Next, the perturbation Ertel q' is partitioned into N parts, where $\sum_{n=1}^{N} q_n = q'$. PPVI is then conducted by inverting each individual q_n for the balanced geopotential (Φ_n) and streamfunction (Ψ_n) perturbations that can be attributed to q_n, which requires the use of linear perturbation forms of Eqs. (3) and (4) (Davis and Emanuel 1991):

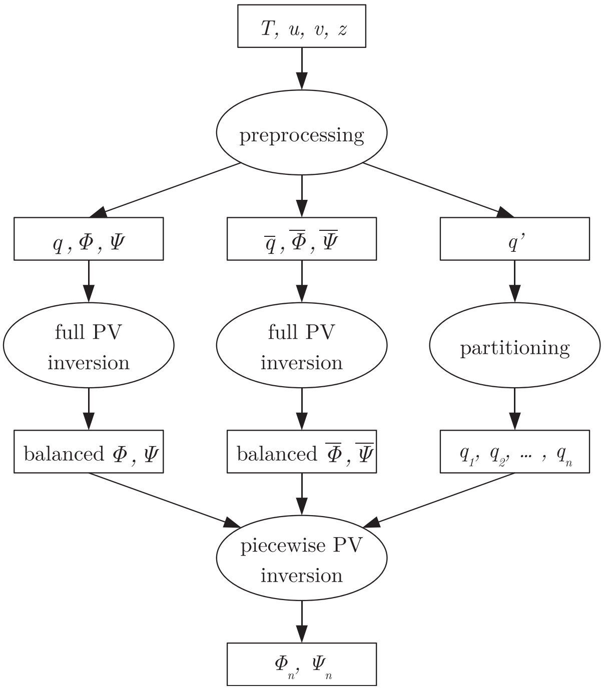

FIG. 2. Piecewise potential vorticity inversion computation steps. Rectangles present variables, including temperature T, zonal wind speed u, meridional wind speed v, geopotential height z, potential vorticity q, geopotential Φ, and streamfunction Ψ, and ovals represent computational processes.

$$\nabla^2\Phi_n = \nabla \cdot (f\nabla\Psi) + \frac{2}{a^4\cos^2\phi}\left(\frac{\partial^2\Psi^*}{\partial\lambda^2}\frac{\partial^2\Psi_n}{\partial\phi^2} + \frac{\partial^2\Psi^*}{\partial\phi^2}\frac{\partial^2\Psi_n}{\partial\lambda^2} - 2\frac{\partial^2\Psi^*}{\partial\lambda\,\partial\phi}\frac{\partial^2\Psi_n}{\partial\lambda\,\partial\phi}\right) \quad \text{and} \tag{5}$$

$$q_n = \frac{g\kappa\pi}{p}\left[(f + \nabla^2\Psi^*)\frac{\partial^2\Phi_n}{\partial\pi^2} + \frac{\partial^2\Phi^*}{\partial\pi^2}\nabla^2\Psi_n - \frac{1}{a^2\cos^2\phi}\left(\frac{\partial^2\Psi^*}{\partial\lambda\,\partial\pi}\frac{\partial^2\Phi_n}{\partial\lambda\,\partial\pi} + \frac{\partial^2\Phi^*}{\partial\lambda\,\partial\pi}\frac{\partial^2\Psi_n}{\partial\lambda\,\partial\pi}\right) - \frac{1}{a^2}\left(\frac{\partial^2\Psi^*}{\partial\phi\,\partial\pi}\frac{\partial^2\Phi_n}{\partial\phi\,\partial\pi} + \frac{\partial^2\Phi^*}{\partial\phi\,\partial\pi}\frac{\partial^2\Psi_n}{\partial\phi\,\partial\pi}\right)\right], \tag{6}$$

where $(\Phi, \Psi)^* = (\overline{\Phi}, \overline{\Psi}) + 1/2\sum_{n=1}^{N}(\Phi_n, \Psi_n)$. The values of Φ_n and Ψ_n show the vertical distribution of geopotential and streamfunction perturbations that are associated with the perturbation at a particular atmospheric level of interest. The sum of all balanced perturbations equals the total balanced perturbation:

$$\sum_{n=1}^{N}\Phi_n = \Phi' \quad \text{and} \quad \sum_{n=1}^{N}\Psi_n = \Psi'. \tag{7}$$

I then quantify the contribution of each atmospheric layer to relative vorticity at 850 hPa by converting the balanced perturbations Ψ_n of each atmospheric level to relative vorticity (ζ_n):

$$\zeta_n = \nabla^2 \Psi_n . \tag{8}$$

Finally, the ζ_n fields are resampled to T42 to make results comparable to T42ζ_{850} used in TRACK (Hijmans 2016).

I apply PPVI to intense ETC tracks with T42$\zeta_{850} \geq 10 \times 10^{-5} \mathrm{s}^{-1}$. The inversion is conducted for the four ETC centers that occur 36, 24, 12, and 0 h prior to maximum ETC intensity. The spatial domain of each inversion consists of a rectangle that extends 15° latitude north and south, and 20° longitude east and west of the ETC center of interest (Fig. 1).

Two different techniques are used to partition q'. The first approach partitions q' into a surface layer (1000 hPa), the lower atmospheric layer (850 and 700 hPa), and the upper atmospheric layer (500, 400, 300, 250, 200, 150, and 100 hPa) (Davis and Emanuel 1991). This approach is implemented for all four ETC centers that occur 36, 24, 12, and 0 h prior to maximum ETC intensity, and is referred to as pressure-based partitioning, hereafter. The second approach uses relative humidity (RH) as an additional criterion next to pressure to partition q', which makes it possible to compute contributions associated with boundary potential temperature anomalies close to the surface (θ_B), condensational heating in the lower-level atmosphere (q_{sat}), and stratospheric intrusion in the upper-level atmosphere (q_{tr}) (Davis 1992). The computation of θ_B, q_{sat}, and q_{tr} is first implemented for a random sample of 100 ETCs (see section 2d for details), and then for all 3273 ETCs for the instance of maximum ETC intensity.

Contributions correspond to values along a vertical line that is centered on the location of maximum T42ζ_{850} computed from the balanced flow. The precise location is determined by searching for the maximum value within a 4° × 4° window around the ETC center computed from the full flow. This is necessary as the location of T42ζ_{850} may slightly differ between the full and balanced flows.

d. Sensitivity experiments

To assess the robustness of my results to different methodological settings, I conduct four additional experiments for a random sample of 100 ETCs. The four experiments are compared to a standard experiment (STAN) that is based on the same methodological settings as the main runs applied to the sample of 100 ETCs. The first additional experiment (MEAN) computes the contributions from the different atmospheric layers by averaging the values within the 4° × 4° window rather than by assessing contributions along a vertical line. The second experiment (INVZ) computes contributions for geopotential height at 1000 hPa rather than for the streamfunction at 850 hPa. The motivation behind this experiment is the concern that q perturbations at the lower level (700–850 hPa) could present the strongest contribution to the 850-hPa streamfunction simply due to spatial coincidence. The third experiment (CLIM) uses a climatological mean value rather than a 5-day mean value for the background flow.

The fourth experiment (RHUM) is based on the refined q' partitioning that uses RH in addition to pressure to separate contributions. Contributions associated with θ_B, q_{sat}, and q_{tr} equal contributions that originate from the surface (1000 hPa), the lower-level atmosphere (700–850 hPa), and the upper-level atmosphere (100–500 hPa), respectively, as long as RH in the lower level is equal to or greater than 70%. If RH at 850 hPa is less than 70%, then the contributions at this level are associated with θ_B. Similarly, if RH at 700 hPa is less than 70%, the contributions at this level are associated with q_{tr}. This RH-based partitioning is more meaningful compared to the pressure-based partitioning, as it provides a more accurate separation of contributions associated with θ_B, q_{sat}, and q_{tr}. The results will show that the RH-based partitioning does lead to slightly different results compared to the pressure-based partitioning. I, therefore, also apply the RH-based partitioning to all 3273 ETCs for the instance of maximum ETC intensity.

3. Results

a. Storm intensity

Tracking all ETCs north of 30° latitude from 1980 to 2016 (49 165 ETCs) shows that the most frequent maximum T42ζ_{850} value present in all ETC tracks is $3.9 \times 10^{-5} \mathrm{s}^{-1}$, with a 95th percentile of $10.6 \times 10^{-5} \mathrm{s}^{-1}$ (not shown). Based on this observation, I define an intense ETC as a storm that has at least one ETC center with T42$\zeta_{850} \geq 10 \times 10^{-5} \mathrm{s}^{-1}$ (3431 events, or 7% of all ETCs). The vast majority of these intense ETCs are marine cyclones that travel across the North Pacific and North Atlantic during the cold season (Fig. 1a). A small portion of these storms (158 events) either are located north of 72° latitude or occur during the first or last three days of the year, and are therefore excluded from this analysis (see section 2 for details). All remaining 3273 participate in the PPVI that is described next.

b. Potential vorticity structure

Vertical cross sections of storm-centered composites averaged over all intense 3273 ETCs show the presence of a positive upper-level q' west of the ETC center [1.5 potential vorticity units (PVU; 1 PVU = 10^{-6} K kg^{-1} m^2 s^{-1}); red

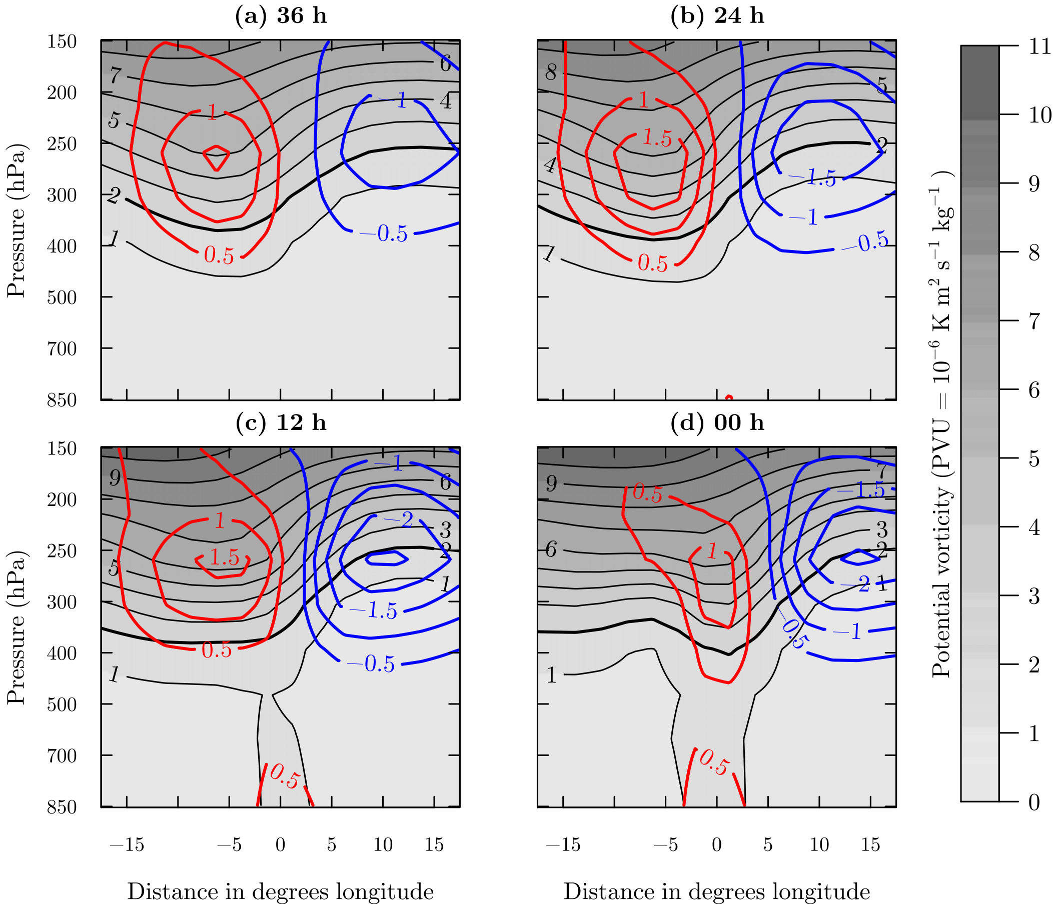

FIG. 3. Vertical cross sections of instantaneous potential vorticity q of ETC centered composites (a) 36, (b) 24, (c) 12, and (d) 0 h prior to maximum T42ζ_{850}. The bold lines present the dynamical tropopause at 2 PVU, and the red and blue contours are positive and negative values for q perturbations (q'), respectively.

contours] and a negative upper-level q' east of the ETC center (−1.0 PVU; blue contours) 36 h prior to maximum ETC intensity (Fig. 3a). As ETC intensity increases, the upper-level positive q' moves eastward relative to the ETC center until it is located vertically above the ETC center during the instance of maximum ETC intensity (Fig. 3d). The same composites also show an undulation of the 2-PVU dynamical tropopause that enhances with increasing ETC intensity, which indicates stratospheric intrusion. Also, a potential vorticity tower (1 PVU) and a lower-level positive q' (0.5 PVU) that is associated with condensational heating from above, develop 12 h prior to maximum T42ζ_{850} (Fig. 3c).

The corresponding horizontal cross sections for the instance of maximum T42ζ_{850} show a positive surface θ' of 3 K west of the ETC center. This θ' acts as a surrogate q' and is caused by warm air advection to the northeast and cold air advecting to the southwest of the ETC center, deforming the 1000-hPa isentropes (Fig. 4a). At the lower level (700–850 hPa) a positive q' of 0.4 PVU associated with condensational heating forms at the ETC center (Fig. 4b). At the upper level (100–500 hPa) a stronger q' related to stratospheric intrusion forms southwest of the ETC center with a value of 1.0 PVU (Fig. 4c). The importance of the surface θ', the lower-level q', and the upper-level q' for ETC intensity is investigated through PPVI below.

c. *Contributions from pressure-based partitioning*

Results from PPVI show that about half of the ETC intensity (i.e., perturbed maximum T42ζ_{850}) is caused by the lower-level (700–850 hPa) q' (51%; 4.9×10^{-5}s^{-1}) (Fig. 4e). Contributions from the upper level (100–500 hPa) and from the surface (1000 hPa) are much less, namely 26% (2.5×10^{-5}s^{-1}) and 22% (2.1×10^{-5}s^{-1}), respectively (Figs. 4d,f). The sum of contributions together with the 5-day mean background flow (Fig. 4g) resembles the balanced flow (see section 2 for details), confirming that the values produced by PPVI are internally consistent (Figs. 4h,i).

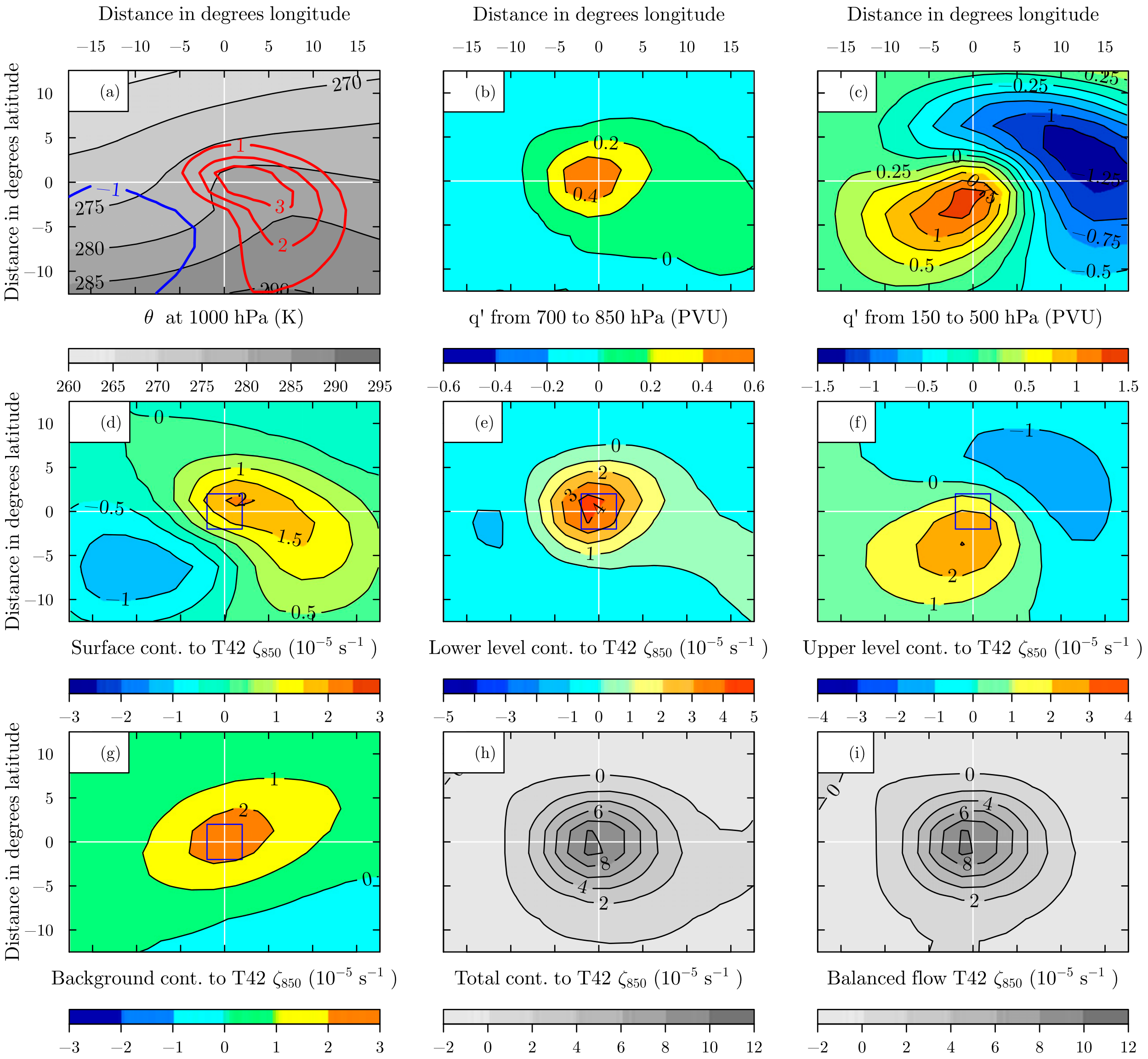

FIG. 4. ETC centered horizontal composites averaged over 3273 ETCs of (a) θ (filled contours) and θ' (red and blue contours) at the surface and q' at the (b) lower level and (c) upper level. (d)–(f) The corresponding contributions to maximum T42ζ_{850}. (g) The background flow at 850 hPa, (h) the sum of the background flow and the contributions from all levels, and (i) the balanced flow at 850 hPa. The white crosses mark the location of the ETC center and the blue boxes in (c)–(h) show a 4° × 4° search window that is used to compute contributions.

The contributions described above vary during the different developmental stages of ETCs. The average value of intense ETCs T42ζ_{850} of intense ETCs increases from $5.9 \times 10^{-5} s^{-1}$ to $12.3 \times 10^{-5} s^{-1}$ within 36 h (Fig. 5a). The balanced flow T42ζ_{850} (pyramid) closely resembles the corresponding values of the full flow (asterisk), suggesting that the balance conditions outlined in the methods section (section 2) provide a good approximation for the full flow. The average differences between both flows is 5.6% with respect to T42ζ_{850}. The increase in T42ζ_{850} is supported by all three q perturbations and the background flow. The background flow may differ among time steps as the location of the ETC also changes with time.

Relative contributions to perturbed T42ζ_{850} that originate from the surface decrease from 34% to 22% within the last 24 h, while upper-level contributions increase from 15% to 26% during the last 12 h (Fig. 5b). Relative contributions from the lower level, on the other hand, are fairly constant during these 36 h, ranging between 52% and 56% for perturbations. The remaining sections focus on contributions during the instance of maximum ETC intensity.

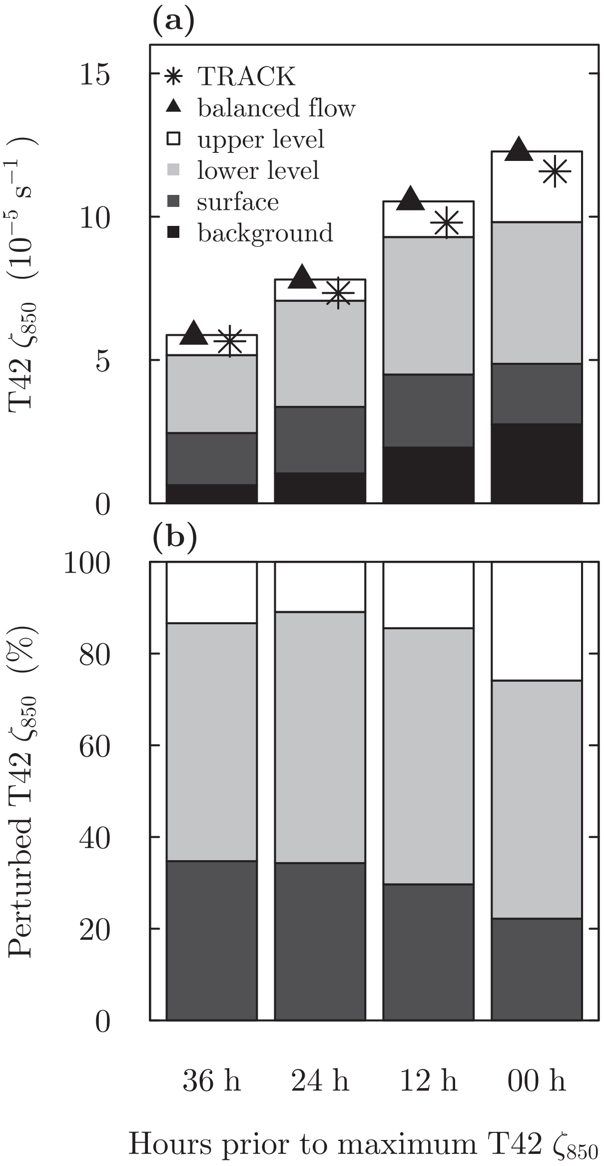

FIG. 5. (a) Contributions from the background flow, the surface, the lower-level atmosphere, and the upper-level atmosphere to T42ζ_{850} for four time steps prior to maximum ETC intensity. Also given are the T42ζ_{850} values of the balanced flow (pyramid) and full flow (asterisk) as computed from the cyclone tracking algorithm TRACK. (b) The relative contributions to perturbed T42ζ_{850}.

d. Sensitivity experiments

Experiments carried out with varying methodological settings for a random sample of 100 ETCs confirm that the largest contribution originates from the lower-level atmosphere, regardless of the chosen methodological setting (Table 1). The corresponding lower-level contributions are 53%, 51%, 51%, and 45% for the experiments MEAN, INVZ, CLIM, and RHUM, respectively. Larger sensitivities exist for contributions from the surface and upper level for the experiment CLIM when compared to STAN (−11% and +15%, respectively). Also, surface contributions increase by 8% in the INVZ experiment, which is balanced by an equal reduction in lower-level and upper-level contributions (4% each). The RH-based partitioning (RHUM) reduces lower-level contributions by 10%, which is almost entirely due to an increase in upper-level contributions rather than surface contributions. Results for RH-based partitioning applied to all 3273 ETCs are presented next.

e. Contributions from relative humidity-based partitioning

Applying the RH-based partitioning to all 3273 ETCs shows that intense storms are primarily driven by q_{sat} (43% of ETC intensity), and only to a lesser extent by q_{tr} (34% of ETC intensity) and θ_B (23% of ETC intensity) (Table 2). Also, q_{sat} dominates contributions most frequently (53% of all ETCs), followed by q_{tr} (36% of all ETCs) and θ_B (11% of all ETCs) (Table 2). The mean contributions stated above are subject to considerable variability. The corresponding interquartile ranges for q_{sat}, q_{tr}, and θ_B are 31%–55%, 21%–47%, and 12%–32%, respectively. This variability is partly due to seasonal and regional differences, which are discussed below.

Most intense ETCs form during the colder months from October to March (78% of all ETCs) (Table 2). The frequency of extreme ETCs is larger in the Pacific compared to the Atlantic (+15 ETCs yr^{-1}) and greater in western compared to eastern ocean basins (+5 ETCs yr^{-1} on average) (Table 2; Fig. 6a). Also, ETC intensity is larger in the Pacific ($+0.2 \times 10^{-5}\,\mathrm{s}^{-1}$), with higher values in the western compared to the eastern part ($+0.4 \times 10^{-5}\,\mathrm{s}^{-1}$) (Table 2; Fig. 6e). The seasonal and regional differences of θ_B, q_{sat}, and q_{tr} contributions are summarized next.

Contributions from θ_B are larger 1) during colder months (26% of ETC intensity) compared to warmer months (13%), 2) in the Atlantic (25%) compared to the Pacific (22%), and 3) in western (24%–26%) compared to eastern ocean basins (20%–23%) (Table 2). Maximum θ_B contributions are located in proximity to the Kuroshio (32%; $3 \times 10^{-5}\,\mathrm{s}^{-1}$) and the Gulf Stream (37%; $4 \times 10^{-5}\,\mathrm{s}^{-1}$), while minimum θ_B contributions are present in the eastern ocean basins (about 13%; $1 \times 10^{-5}\,\mathrm{s}^{-1}$) (Figs. 6b,f). The seasonal and regional frequencies of θ_B-dominated ETCs follow the same pattern as the corresponding contributions. Storms dominated by θ_B are more frequent 1) during colder months (13% of all ETCs that occur from October to March) compared to warmer months (3%), 2) in the Atlantic (15% of all ETCs that occur in the Atlantic) compared to the Pacific (8%), and 3) in western ocean basins (11%–20% of all ETCs that occur in the western

TABLE 1. Mean relative contributions (%) from the surface, the lower-level atmosphere, and the upper-level atmosphere for the experiments STAN, MEAN, INVZ, CLIM, and RHUM conducted for a random sample of 100 ETCs (see section 2 for details). The delta (Δ) shows the corresponding differences when comparing against results from STAN. Statistically significant differences are marked with an asterisk (two-sampled Wilcoxon test at the 5% level; R Core Team 2013).

Expt	Surface	Δ	Lower level	Δ	Upper level	Δ
STAN	21.1	0.0	54.2	0.0	24.8	0.0
MEAN	21.9	0.9	52.7	−1.5	25.4	0.6
INVZ	28.3	7.2*	50.7	−3.5*	21.0	−3.8
CLIM	9.6	−11.4*	51.0	−3.2	39.4	14.6*
RHUM	21.3	0.3	44.5	−9.7*	34.2	9.4*

basins) compared to eastern ocean basins (4%–9%) (Table 2, Fig. 7a).

Contributions from q_{sat} are larger 1) during warmer months (49% of ETC intensity) compared to colder months (41%) and 2) in the Pacific (44%) compared to the Atlantic (39%) (Table 2). Maximum contributions from q_{sat} are located in the North Pacific (53%; $5 \times 10^{-5}\,\mathrm{s}^{-1}$; Figs. 6c,g). The seasonal and regional frequencies of q_{sat}-dominated ETCs follow the same pattern as the corresponding contributions. ETCs dominated by q_{sat} are more frequent 1) during warmer months (61%) compared to colder months (50%) and 2) in the Pacific (56%) compared to the Atlantic (46%) (Table 2; Fig. 7b).

Contributions from q_{tr} are larger 1) during warmer months (38% of ETC intensity) compared to colder months (33%), 2) in the Atlantic (36%) compared to the Pacific (34%), and 3) in eastern (35%–37%) compared to western ocean basins (32%–34%) (Table 2). Maximum contributions from q_{tr} are located in the eastern part of the ocean basins, reaching 46% ($4 \times 10^{-5}\,\mathrm{s}^{-1}$) in the eastern Pacific and 53% ($5 \times 10^{-5}\,\mathrm{s}^{-1}$) in the eastern Atlantic (Figs. 6d,h). No significant seasonal or regional differences were found for the frequencies of ETCs with dominant contributions from q_{tr} (Table 2; Fig. 7c).

4. Discussion

This study presents the first climatological assessment of potential vorticity perturbations and their contributions to the intensity of extreme ETCs in the Northern Hemisphere. Results show that in about half of all cases the largest contributions during maximum ETC intensity are associated with q_{sat} (53% of all ETCs), followed by q_{tr} (36%) and θ_B (11%). The importance of q_{sat} and θ_B varies among seasons and ocean basins. The relative frequency of storms that are dominated by q_{sat} is larger during warmer months compared to colder months and in the Pacific compared to the Atlantic. The exact opposite pattern applies to storms dominated by θ_B. Furthermore, the relative frequency of

TABLE 2. ETC sample size (N), annual mean frequency, ETC intensity ($\mathrm{T42}\zeta_{850}$), and relative contributions to $\mathrm{T42}\zeta_{850}$ perturbations from boundary potential temperature anomalies close to the surface (θ_B), condensational heating (q_{sat}), and stratospheric intrusion (q_{tr}) during the instance of maximum ETC intensity. Also shown is the percentage of ETCs whose contributions are dominated either by θ_B, q_{sat}, or q_{tr}. Numbers in parentheses give the corresponding interquartile range. Statistically significant differences between mean values are marked with an asterisk (two-sampled Wilcoxon test at the 5% level; R Core Team 2013).

				Relative contributions (%)			Dominant contributions (%)		
Region	N	Frequency yr^{-1}	$\mathrm{T42}\zeta_{850} 10^{-5}\mathrm{s}^{-1}$	θ_B	q_{sat}	q_{tr}	θ_B	q_{sat}	q_{tr}
NH	3273	88 (84–94)	11.6 (10.5–12.3)	23 (12–32)	43 (31–55)	34 (21–47)	11 (8–13)	53 (49–55)	36 (33–40)
NH Oct–Mar	2537	69 (64–74)	11.7 (10.6–12.4)	26 (15–34)	41 (30–53)	33 (20–46)	13 (9–17)	50 (46–54)	36 (33–40)
NH Apr–Sep	736	20 (17–22)	11.3 (10.4–11.8)	13 (5–21)	49 (36–63)	38 (24–52)	3 (0–5)	61 (54–68)	36 (29–41)
Difference	1801	49*	0.4*	13*	−8*	−5*	10*	−11*	0
Pacific	1809	49 (45–52)	11.7 (10.6–12.6)	22 (13–30)	44 (33–56)	34 (21–46)	8 (4–11)	56 (52–61)	36 (32–38)
Atlantic	1245	34 (30–38)	11.5 (10.5–12.2)	25 (13–35)	39 (27–52)	36 (20–50)	15 (11–21)	46 (38–50)	39 (33–45)
Difference	564	15*	0.2*	−3*	5*	−2*	−7*	11*	−3
Western Pacific	973	26 (25–29)	11.9 (10.7–12.8)	24 (14–33)	44 (32–57)	32 (19–45)	11 (7–16)	55 (48–62)	34 (29–40)
Eastern Pacific	836	23 (19–26)	11.5 (10.5–12.2)	20 (12–27)	45 (34–56)	35 (22–47)	4 (0–7)	58 (52–65)	38 (30–41)
Difference	137	4*	0.4*	4*	−1	−3*	6*	−3	−4
Western Atlantic	729	20 (17–22)	11.5 (10.5–12.2)	26 (12–39)	39 (28–51)	34 (19–48)	20 (13–29)	43 (35–52)	37 (29–45)
Eastern Atlantic	516	14 (11–17)	11.5 (10.5–12.1)	23 (13–32)	40 (27–52)	37 (22–52)	9 (0–13)	50 (41–58)	42 (30–53)
Difference	213	6*	0.0	3*	0	−3*	11*	−7	−5

(a) ETC frequency (b) θ_B (absolute) (c) q_{sat} (absolute) (d) q_{tr} (absolute)

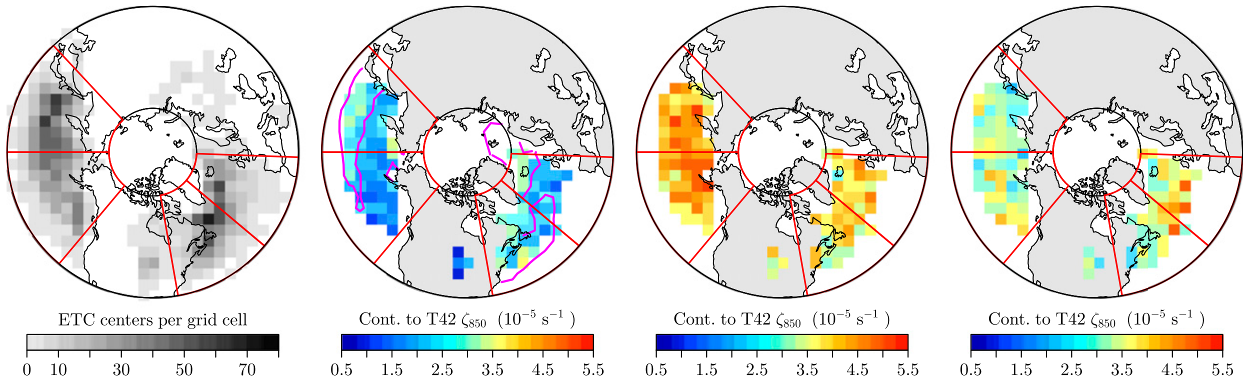

(e) ETC intensity (f) θ_B (relative) (g) q_{sat} (relative) (h) q_{tr} (relative)

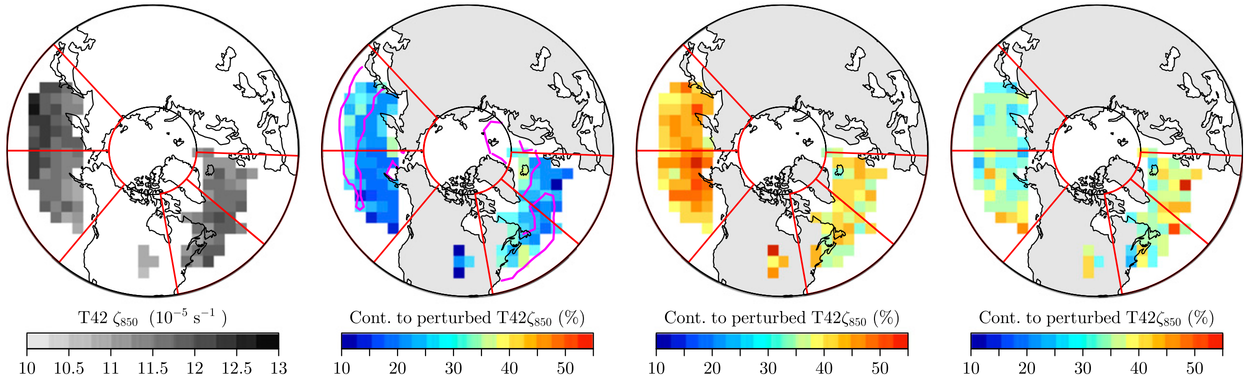

FIG. 6. (a) Total frequency of ETC centers with maximum T42ζ_{850} per grid cell (500 km × 500 km) (3273 events) and (e) corresponding mean maximum T42ζ_{850}. (b)–(d) Absolute contributions to maximum T42ζ_{850} and (f)–(h) the corresponding relative contributions. Grid cells with less than 10 ETC centers are excluded in (b) to (h). The red lines denote the boundaries of western and eastern ocean basins used in Table 2. The magenta contours in (b) and (f) enclose regions where the horizontal gradient of the climatological mean sea surface temperature from October to March exceeds 1 K 100 km^{-1} during the 1980–2016 period.

θ_B-dominated storms is larger in western compared to eastern ocean basins.

These values apply to the instance of maximum ETC intensity, and are not necessarily representative for conditions during early stages of ETC cyclogenesis. The applicability of PPVI is limited during early ETC development, since all contributions are computed vertically. This may cause an underestimation of upper-level and surface contributions when positive q perturbations interact along a tilted axis that is centered at maximum T42ζ_{850}. PPVI results are, therefore, most reliable during the instance of maximum ETC intensity when all three perturbations are vertically aligned.

Contributions from the surface layer and the upper-level atmosphere are sensitive to the definition of the background flow. The two definitions used in this study are a 5-day mean and a climatological mean. Although the first approach has been widely adopted (Davis and Emanuel 1991; Davis 1992; Huo et al. 1999; Stoelinga 1996; Martin and Otkin 2004), the sensitivity of PPVI to the background flow should be explored in greater detail. This could be done by systematically increasing the time window that is used for computing the background flow. Such an analysis could show how exactly the background affects the inversion and whether a 5-day mean value leads to the most meaningful results.

The seasonal and regional differences of ETC frequencies that are dominated by θ_B and q_{sat} could be explored in more detail in a range of numerical experiments. Such experiments could assess 1) whether the strong contributions from θ_B during the cold season is related to the enhanced temperature difference between the sea surface and the air, 2) whether the high frequency of θ_B-dominated ETCs in the western ocean basins is caused by strong sea surface temperature gradients associated with the western boundary currents, and 3) to what extent the relative high frequency of q_{sat}-dominated ETCs during warmer months can be explained by the Clausius–Clapeyron relationship.

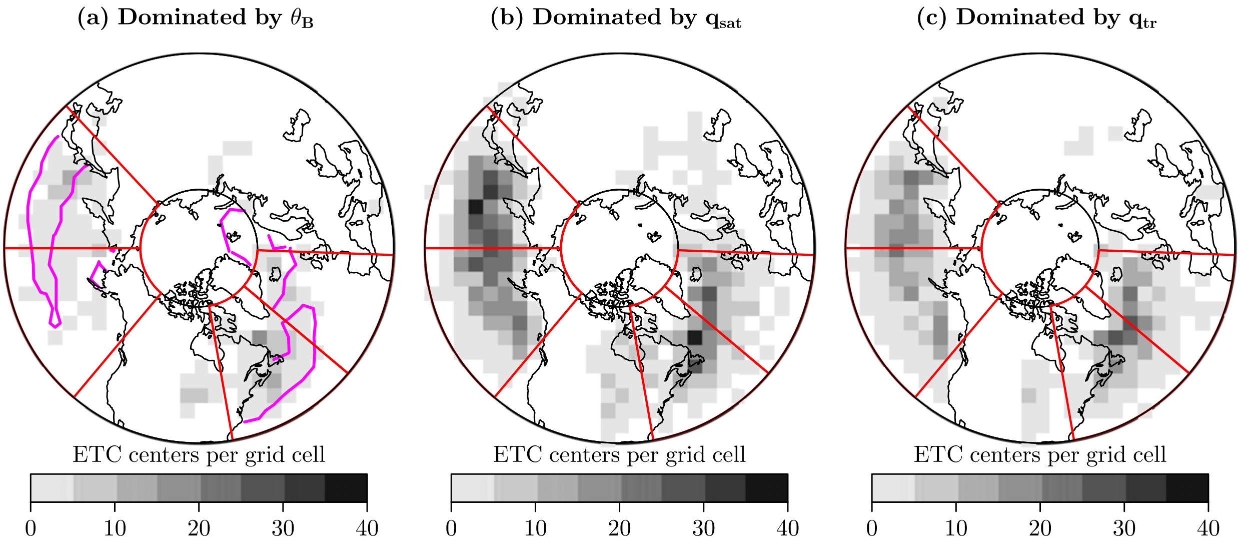

FIG. 7. Total frequency of ETCs per grid cell (500 km × 500 km) (3273 events) that are dominated by (a) surface temperature anomalies (θ_B), (b) condensational heating (q_{sat}), and (c) stratospheric intrusion (q_{tr}). The red lines denote the boundaries of western and eastern ocean basins used in Table 2. The magenta contours in (a) enclose regions where the horizontal gradient of the climatological mean sea surface temperature from October to March exceeds 1 K 100 km^{-1} during the 1980–2016 period.

The dominant role of condensational heating during the instance of maximum ETC intensity may have important implications for ETC biases and projected future changes in GCMs. Regional climate model (RCM) experiments show that latent heat release and ETC intensity become stronger when increasing the horizontal model resolution from 120 to 20 km (Willison et al. 2013). Downscaling the GCM CanESM2 with the RCM CanRCM4 increases the frequency of rapidly intensifying ETCs by one-third and associated precipitation by 22% (Seiler et al. 2018). The tendency of GCMs to simulate ETCs that are too weak (Zappa et al. 2013a; Seiler and Zwiers 2016a) may, therefore, be related to weak condensational heating that is limited by the modest spatial resolution of GCMs. This could be verified by conducting PPVI for ETCs simulated in GCMs for the historic period and by comparing the results to the findings presented in this study. Repeating the same experiment under a scenario with projected future GHG concentrations would show whether biases in condensational heating affect the projected changes and how projected changes can be understood from the potential vorticity perspective. Conducting PPVI for GCM data would greatly improve our current understanding of the physical mechanisms that cause ETC biases and projected future changes in GCMs. This may provide guidance for improving model performance and reducing uncertainties associated with future projections.

Acknowledgments. I am very grateful for the technical support from and discussions with Chris Davis (National Center for Atmospheric Research), Kevin I. Hodges (University of Reading), Ryan Torn (University at Albany), and Francis W. Zwiers (Pacific Climate Impacts Consortium, University of Victoria). I acknowledge the use of ERA-Interim data produced by the European Centre for Medium-Range Weather Forecasts. I wish to thank three anonymous reviewers for their helpful comments.

REFERENCES

Anderson, D., K. I. Hodges, and B. J. Hoskins, 2003: Sensitivity of feature-based analysis methods of storm tracks to the form of background field removal. *Mon. Wea. Rev.*, **131**, 565–573, https://doi.org/10.1175/1520-0493(2003)131<0565:SOFBAM>2.0.CO;2.

Butler, A. H., D. W. Thompson, and R. Heikes, 2010: The steady-state atmospheric circulation response to climate change–like thermal forcings in a simple general circulation model. *J. Climate*, **23**, 3474–3496, https://doi.org/10.1175/2010JCLI3228.1.

Čampa, J., and H. Wernli, 2012: A PV perspective on the vertical structure of mature midlatitude cyclones in the Northern Hemisphere. *J. Atmos. Sci.*, **69**, 725–740, https://doi.org/10.1175/JAS-D-11-050.1.

Collins, M., and Coauthors, 2013: Long-term climate change: Projections, commitments and irreversibility. *Climate Change 2013: The Physical Science Basis*, T. F. Stocker et al., Eds., Cambridge University Press, 1029–1136.

Dacre, H. F., and S. L. Gray, 2009: The spatial distribution and evolution characteristics of North Atlantic cyclones. *Mon. Wea. Rev.*, **137**, 99–115, https://doi.org/10.1175/2008MWR2491.1.

Davis, C. A., 1992: A potential-vorticity diagnosis of the importance of initial structure and condensational heating in observed extratropical cyclogenesis. *Mon. Wea. Rev.*, **120**, 2409–2428, https://doi.org/10.1175/1520-0493(1992)120<2409:APVDOT>2.0.CO;2.

——, and K. A. Emanuel, 1991: Potential vorticity diagnostics of cyclogenesis. *Mon. Wea. Rev.*, **119**, 1929–1953, https://doi.org/10.1175/1520-0493(1991)119<1929:PVDOC>2.0.CO;2.

Dee, D., and Coauthors, 2011: The ERA-Interim reanalysis: Configuration and performance of the data assimilation system. *Quart. J. Roy. Meteor. Soc.*, **137**, 553–597, https://doi.org/10.1002/qj.828.

Deveson, A., K. Browning, and T. Hewson, 2002: A classification of FASTEX cyclones using a height-attributable quasi-geostrophic vertical-motion diagnostic. *Quart. J. Roy. Meteor. Soc.*, **128**, 93–117, https://doi.org/10.1256/00359000260498806.

Fink, A. H., T. Brücher, V. Ermert, A. Krüger, and J. G. Pinto, 2009: The European storm Kyrill in January 2007: Synoptic evolution, meteorological impacts and some considerations with respect to climate change. *Nat. Hazards Earth Syst. Sci.*, **9**, 405–423, https://doi.org/10.5194/nhess-9-405-2009.

Graf, M. A., H. Wernli, and M. Sprenger, 2017: Objective classification of extratropical cyclogenesis. *Quart. J. Roy. Meteor. Soc.*, **143**, 1047–1061, https://doi.org/10.1002/qj.2989.

Gray, S. L., and H. F. Dacre, 2006: Classifying dynamical forcing mechanisms using a climatology of extratropical cyclones. *Quart. J. Roy. Meteor. Soc.*, **132**, 1119–1137, https://doi.org/10.1256/qj.05.69.

Hijmans, R. J., 2016: raster: Geographic Data Analysis and Modeling. r package version 2.5-8, https://CRAN.R-project.org/package=raster.

Hodges, K., 1994: A general method for tracking analysis and its application to meteorological data. *Mon. Wea. Rev.*, **122**, 2573–2586, https://doi.org/10.1175/1520-0493(1994)122<2573:AGMFTA>2.0.CO;2.

——, 1999: Adaptive constraints for feature tracking. *Mon. Wea. Rev.*, **127**, 1362–1373, https://doi.org/10.1175/1520-0493(1999)127<1362:ACFFT>2.0.CO;2.

——, and Coauthors, 1995: Feature tracking on the unit sphere. *Mon. Wea. Rev.*, **123**, 3458–3465, https://doi.org/10.1175/1520-0493(1995)123<3458:FTOTUS>2.0.CO;2.

Hoskins, B. J., M. McIntyre, and A. W. Robertson, 1985: On the use and significance of isentropic potential vorticity maps. *Quart. J. Roy. Meteor. Soc.*, **111**, 877–946, https://doi.org/10.1002/qj.49711147002.

Huo, Z., D.-L. Zhang, and J. R. Gyakum, 1999: Interaction of potential vorticity anomalies in extratropical cyclogenesis. Part I: Static piecewise inversion. *Mon. Wea. Rev.*, **127**, 2546–2562, https://doi.org/10.1175/1520-0493(1999)127<2546:IOPVAI>2.0.CO;2.

Lunkeit, F., K. Fraedrich, and S. Bauer, 1998: Storm tracks in a warmer climate: Sensitivity studies with a simplified global circulation model. *Climate Dyn.*, **14**, 813–826, https://doi.org/10.1007/s003820050257.

Martin, J. E., 2013: *Mid-Latitude Atmospheric Dynamics: A First Course*. John Wiley & Sons, 336 pp.

——, and J. A. Otkin, 2004: The rapid growth and decay of an extratropical cyclone over the central Pacific Ocean. *Wea. Forecasting*, **19**, 358–376, https://doi.org/10.1175/1520-0434(2004)019<0358:TRGADO>2.0.CO;2.

Mass, C., and B. Dotson, 2010: Major extratropical cyclones of the northwest United States: Historical review, climatology, and synoptic environment. *Mon. Wea. Rev.*, **138**, 2499–2527, https://doi.org/10.1175/2010MWR3213.1.

Petterssen, S., and S. J. Smebye, 1971: On the development of extratropical cyclones. *Quart. J. Roy. Meteor. Soc.*, **97**, 457–482, https://doi.org/10.1002/qj.49709741407.

R Core Team, 2013: R: A language and environment for statistical computing. R Foundation for Statistical Computing, http://www.R-project.org/.

Seiler, C., and F. Zwiers, 2016a: How well do CMIP5 climate models reproduce explosive cyclones in the extratropics of the Northern Hemisphere? *Climate Dyn.*, **46**, 1241–1256, https://doi.org/10.1007/s00382-015-2642-x.

——, and ——, 2016b: How will climate change affect explosive cyclones in the extratropics of the Northern Hemisphere? *Climate Dyn.*, **46**, 3633–3644, https://doi.org/10.1007/s00382-015-2791-y.

——, ——, K. I. Hodges, and J. Scinocca, 2018: How does dynamical downscaling affect model biases and future projections of explosive extratropical cyclones along North America's Atlantic coast? *Climate Dyn.*, **50**, 677–692, https://doi.org/10.1007/s00382-017-3634-9.

Stoelinga, M. T., 1996: A potential vorticity–based study of the role of diabatic heating and friction in a numerically simulated baroclinic cyclone. *Mon. Wea. Rev.*, **124**, 849–874, https://doi.org/10.1175/1520-0493(1996)124<0849:APVBSO>2.0.CO;2.

Ulbrich, U., G. Leckebusch, and J. Pinto, 2009: Extra-tropical cyclones in the present and future climate: A review. *Theor. Appl. Climatol.*, **96**, 117–131, https://doi.org/10.1007/s00704-008-0083-8.

Whitaker, J. S., L. W. Uccellini, and K. F. Brill, 1988: A model-based diagnostic study of the rapid development phase of the Presidents' Day cyclone. *Mon. Wea. Rev.*, **116**, 2337–2365, https://doi.org/10.1175/1520-0493(1988)116<2337:AMBDSO>2.0.CO;2.

Willison, J., W. A. Robinson, and G. M. Lackmann, 2013: The importance of resolving mesoscale latent heating in the North Atlantic storm track. *J. Atmos. Sci.*, **70**, 2234–2250, https://doi.org/10.1175/JAS-D-12-0226.1.

Woollings, T., J. M. Gregory, J. G. Pinto, M. Reyers, and D. J. Brayshaw, 2012: Response of the North Atlantic storm track to climate change shaped by ocean–atmosphere coupling. *Nat. Geosci.*, **5**, 313–317, https://doi.org/10.1038/ngeo1438.

Zappa, G., L. C. Shaffrey, and K. I. Hodges, 2013a: The ability of CMIP5 models to simulate North Atlantic extratropical cyclones. *J. Climate*, **26**, 5379–5396, https://doi.org/10.1175/JCLI-D-12-00501.1.

——, ——, ——, P. G. Sansom, and D. B. Stephenson, 2013b: A multimodel assessment of future projections of North Atlantic and European extratropical cyclones in the CMIP5 climate models. *J. Climate*, **26**, 5846–5862, https://doi.org/10.1175/JCLI-D-12-00573.1.